ACS OMEGA
Article
Cite This: ACS Omega 2018, 3, 15780−15788
http://pubs.acs.org/journal/acsodf

First-Principles Structural, Mechanical, and Thermodynamic Calculations of the Negative Thermal Expansion Compound $Zr_2(WO_4)(PO_4)_2$

Philippe F. Weck,*,† Eunja Kim,‡ Margaret E. Gordon,† Jeffery A. Greathouse,† Rémi Dingreville,† and Charles R. Bryan†

†Sandia National Laboratories, Albuquerque, New Mexico 87185, United States

‡Department of Physics and Astronomy, University of Nevada Las Vegas, 4505 Maryland Parkway, Las Vegas, Nevada 89124, United States

Supporting Information

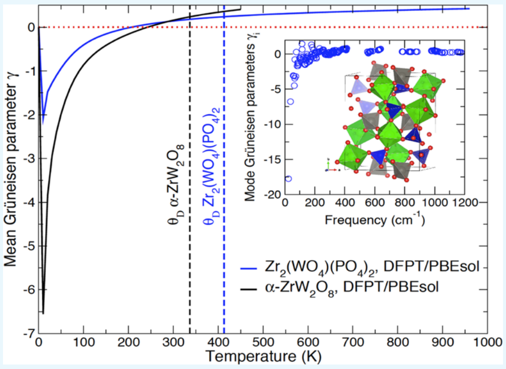

ABSTRACT: The negative thermal expansion (NTE) material $Zr_2(WO_4)(PO_4)_2$ has been investigated for the first time within the framework of the density functional perturbation theory (DFPT). The structural, mechanical, and thermodynamic properties of this material have been predicted using the Perdew, Burke and Ernzerhof for solid (PBEsol) exchange−correlation functional, which showed superior accuracy over standard functionals in previous computational studies of the NTE material α-ZrW_2O_8. The bulk modulus calculated for $Zr_2(WO_4)(PO_4)_2$ using the Vinet equation of state at room temperature is $K_0 = 63.6$ GPa, which is in close agreement with the experimental estimate of 61.3(8) at $T = 296$ K. The computed mean linear coefficient of thermal expansion is -3.1×10^{-6} K^{-1} in the temperature range ∼0−70 K, in line with the X-ray diffraction measurements. The mean Grüneisen parameter controlling the thermal expansion of $Zr_2(WO_4)(PO_4)_2$ is negative below 205 K, with a minimum of −2.1 at 10 K. The calculated standard molar heat capacity and entropy are $C_P^0 = 287.6$ and $S^0 = 321.9$ $J \cdot mol^{-1} \cdot K^{-1}$, respectively. The results reported in this study demonstrate the accuracy of DFPT/PBEsol for assessing or predicting the relationship between structural and thermomechanical properties of NTE materials.

1. INTRODUCTION

Negative thermal expansion (NTE) materials have received considerable experimental and theoretical attention over the past few decades.[1−9] In contrast to most materials, which expand on heating due to anharmonic lattice dynamics,[10] NTE materials contract as the temperature rises, owing to mechanisms ranging from structural/magnetic phase transitions to anomalous vibrational modes (e.g., transverse vibrational modes or rigid unit modes).[3,5,7,8] Well-known examples of NTE materials include silicon, germanium, uranium, β-quartz, elastomers, as well as some framework-structured ceramics and zeolites.[1,3−6,8] NTE materials are often used as thermal-expansion compensators in composites designed to have overall zero or tunable thermal expansion.[7] Precise control of the thermal expansion of materials is critical, for example, in high-precision optical systems, nanoscale semiconductor devices, fuel cells, or high-performance thermoelectric converters.[4,7,8]

Several phases in the Zr/W/O, Zr/V/P/O, and Zr/W/P/O systems have been identified as low or negative thermal expansion materials.[11−28] Among crystalline phases of the Zr/W/P/O system, $Zr_2(WO_4)(PO_4)_2$ was the first reported structure featuring coexistence of WO_4 and PO_4 coordination. $Zr_2(WO_4)(PO_4)_2$ was originally synthesized by Martinek and Hummel[29] as the ternary compound $2ZrO_2 \cdot WO_3 \cdot P_2O_5$ and characterized by Tsvigunov and Sirotinkin.[30] Using room-temperature powder X-ray diffraction (XRD) data, Evans et al.[31] fully solved the structure of $Zr_2(WO_4)(PO_4)_2$, which crystallizes in the orthorhombic space group *Pbcn* (IT no. 60, setting no. 3 *Pnca* (*c*, *a*, *b*); $a = 9.35451(9)$, $b = 12.31831(9)$, and $c = 9.16711(8)$ Å; $Z = 4$), with corner-sharing ZrO_6 octahedral and WO_4 and PO_4 tetrahedral coordination units. This structure is related to the phases $A_2(MO_4)_3$ (with M = Mo, A = Al, Sc, Cr, Fe, Y, In, Ho, Er, Tm, Yb, and Lu, or with M = W, A = Al, Sc, Fe, In, Y, Gd, Tb, Dy, Ho, Yb, Tm, Yb, and Lu) which adopt the orthorhombic *Pbcn*/*Pnca* or monoclinic $P2_1/a$ arrangements.

As shown in dilatometer and XRD studies, orthorhombic $Zr_2(WO_4)(PO_4)_2$ exhibits unusual NTE over a broad temperature range from below room-temperature up to ∼1373 K, without phase transition at atmospheric pressure.[32−37] As discussed by Evans et al.,[32] NTE in both $A_2(MO_4)_3$- and

Received: September 20, 2018
Accepted: November 6, 2018
Published: November 20, 2018

ZrW_2O_8-type structures stems from the transverse thermal motion of bridging O atoms in A−O−M or Zr−O−W linkages. Owing to its remarkable thermal stability, $Zr_2(WO_4)(PO_4)_2$ is often combined with other NTE materials in the fabrication of a variety of NTE composites (e.g., $Zr_2(WO_4)(PO_4)_2/ZrW_2O_8$ or $Zr_2(WO_4)(PO_4)_2/ZrV_{0.6}P_{1.4}O_7$).[38−40]

However, synthesis of $Zr_2(WO_4)(PO_4)_2$ with consistent and well-controlled NTE properties has revealed to be challenging. Evans et al.[32] reported mean linear coefficients of thermal expansion (CTE) of -6×10^{-6} and -3×10^{-6} K^{-1} using dilatometer and XRD measurements, respectively, in the temperature range ∼50−450 K. Cetinkol and Wilkinson[34] obtained a value of -5×10^{-6} K^{-1} from neutron diffraction data between 60 and 300 K and Isobe et al. measured a value of -3.4×10^{-6} K^{-1} in the range ∼300−875 K. Recently, values of -2.36×10^{-6} and -2.61×10^{-6} K^{-1} were estimated by Liu et al. in the temperature range ∼300−1000 K for $Zr_2(WO_4)(PO_4)_2$ samples sintered at 1573 and 1673 K, respectively. Such differences in CTE can be ascribed to the different porosities or average grain sizes resulting from sintering conditions and synthesis reactions[32−37] as well as to possible pressure-induced phase transformations[41] during sample fabrication. Apart from these CTE experimental estimates, very limited information is available on the mechanical and thermodynamic properties of $Zr_2(WO_4)(PO_4)_2$, and no computational studies of this NTE material have been conducted, to the best of our knowledge.

In this work, the orthorhombic phase of $Zr_2(WO_4)(PO_4)_2$ has been investigated for the first time within the framework of the density functional perturbation theory (DFPT). Specifically, the structural, mechanical, and thermodynamic properties of this material have been predicted using the exchange−correlation (XC) functional parameterized by Perdew, Burke, and Ernzerhof for solids (PBEsol),[42] which showed superior accuracy over standard functionals in recent density functional studies of the NTE material α-ZrW_2O_8.[43,44] As demonstrated in previous studies, lattice dynamics simulations using density functional theory (DFT) approaches can provide invaluable information on the structure−properties relationship of NTE materials.[43−46] As limited experimental data exist on the mechanical and thermodynamic properties of $Zr_2(WO_4)(PO_4)_2$, results predicted in this study have also been systematically compared to measured and calculated properties of α-ZrW_2O_8.

Analysis and discussion of our results are given in Section 2, followed by a summary of our findings and conclusions in Section 3. Details of our computational approach are provided in Section 4.

2. RESULTS AND DISCUSSION

2.1. Crystal Structure.

Figure 1 shows the XRD pattern simulated from the relaxed crystal structure optimized with DFT in this study, along with the room-temperature powder XRD pattern of the orthorhombic $Zr_2(WO_4)(PO_4)_2$ structure (space group *Pbcn*) characterized by Evans et al.[31] (Cu Kα radiation, λ = 1.5406 Å). Excellent overall agreement is achieved between the simulated and measured XRD patterns, without noticeable peak shift of 2θ values.

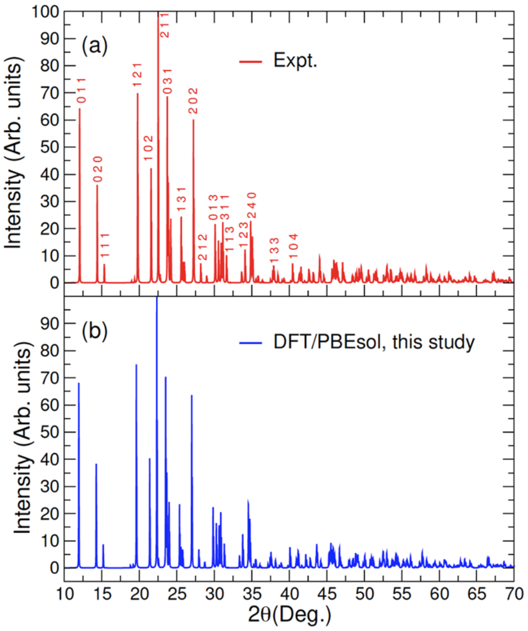

Figure 1. (a) Observed room-temperature powder XRD pattern of $Zr_2(WO_4)(PO_4)_2$ (Cu Kα radiation, λ = 1.5406 Å) (ref 31) and (b) XRD pattern simulated from the relaxed crystal structure optimized with DFT at the GGA/PBEsol level of theory. Major observed reflections are indexed in the *hkl* representation.

The orthorhombic $Zr_2(WO_4)(PO_4)_2$ structure optimized with generalized gradient approximation (GGA)/PBEsol at T = 0 K possesses crystal unit-cell parameters of a = 9.432, b = 12.432, and c = 9.250 Å (b/a = 1.318, c/a = 0.981; V = 1084.59 Å^3). Owing to NTE and to the fact that GGA functionals typically overestimate bond distances, the unit-cell volume predicted in the athermal limit is ∼2.3% larger than the estimate of V = 1059.34(4) Å^3 (a = 9.3640(3), b = 12.3243(4), and c = 9.1793(3) Å; b/a = 1.3161, c/a = 0.9803) obtained at T = 60 K by Cetinkol and Wilkinson[34] using neutron diffraction data. As reported in Table 1, these predicted lattice constants remain close to neutron data[34] at T = 296 K [a = 9.3462(3), b = 12.3313(4), and c = 9.1606(3) Å; b/a = 1.3194, c/a = 0.9801; V = 1055.77(4) Å^3], and the powder XRD data measured by Evans et al.[31] at T = 300 K [a = 9.35451(9), b = 12.31831(9), and c = 9.16711(8) Å; b/a = 1.3168, c/a = 0.9800; V = 1056.34 Å^3].

Ball-and-stick representations of the optimized orthorhombic $Zr_2(WO_4)(PO_4)_2$ structure down the [001], [010], and [100] axes are shown in Figure 2 and selected bond distances and angles calculated with DFT and measured by Evans et al.[31] using room temperature powder XRD are summarized in Table 2.

As described by Evans and coworkers,[31] the orthorhombic $Zr_2(WO_4)(PO_4)_2$ phase is made up of corner-sharing ZrO_6 octahedral and WO_4 and PO_4 tetrahedral coordination units. Each ZrO_6 octahedron is connected to four PO_4 and two WO_4 units. Unlike α-ZrW_2O_8 which features two distinct WO_4 tetrahedral coordination units, all WO_4 units in $Zr_2(WO_4)(PO_4)_2$ are crystallographically equivalent. W atoms occupy 4*c* Wyckoff sites (0.2 symmetry), whereas Zr, P, and O atoms are all positioned on 8*d* Wyckoff sites (1 symmetry). The average O−Zr, O−W, and O−P bond distances are predicted to be 2.085, 1.783, and 1.537 Å, respectively, which are in good agreement with the XRD estimates of 2.087, 1.767, and 1.500 Å (see Table 2). These values are also in line with the average O−Zr, O−W1, and O−W2 bond distances of 2.084, 1.799, and 1.787 Å, respectively, calculated for α-ZrW_2O_8 using PBEsol.[44] The large difference between coordination distances at the W and P sites directly reflects the difference in cation

Table 1. Lattice Parameters and Volume of Orthorhombic $Zr_2(WO_4)(PO_4)_2$ Unit Cell (Space Group *Pbcn*, IT No. 60; Z = 4) Calculated with DFT and Determined from Powder X-ray and Neutron Diffraction Data

method	*T* (K)	*a* (Å)	*b* (Å)	*c* (Å)	*V* (Å^3)
DFT[a]	0	9.432	12.432	9.250	1084.59
expt[b]	300	9.35451(9)	12.31831(9)	9.16711(8)	1056.34
expt[c]	60	9.3640(3)	12.3243(4)	9.1793(3)	1059.34(4)
expt[c]	296	9.3462(3)	12.3313(4)	9.1606(3)	1055.77(4)

[a] This study. [b] Evans et al.; ref 31; powder XRD. [c] Cetinkol and Wilkinson; ref 34; neutron diffraction.

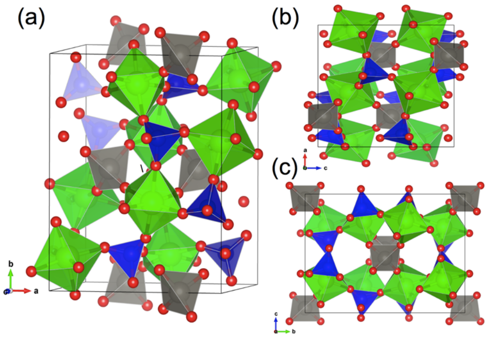

Figure 2. Orthorhombic crystal unit cell of $Zr_2(WO_4)(PO_4)_2$ [space group *Pbcn*, IT no. 60, setting no. 3 *Pnca* (*c*, *a*, *b*); *Z* = 4], with corner-sharing ZrO_6 (green) octahedral and WO_4 (grey) and PO_4 (blue) tetrahedral coordination units, optimized using DFT with GGA/PBEsol. Views along the (a) [001], (b) [010], and (c) [100] directions. Color legend: O, red; P, blue; W, grey; Zr, green.

ionic radii. Both calculated and measured tetrahedral O−W−O and O−P−O and octahedral O−Zr−O angles are close to the ideal values of 109.5 and 90.0°, respectively. The optimized (measured) ZrO_6 octahedral units have a volume of 11.979 (11.995) Å^3, a bond length distortion index of 0.022 (0.026), a quadratic elongation of 1.006 (1.008), a bond angle variance of 20.4$^{\circ 2}$ (24.4$^{\circ 2}$), and an effective coordination of 5.87 (5.83). The calculated (measured) WO_4 and PO_4 tetrahedral units are characterized by volumes of 2.909 (2.820) and 1.863 (1.731) Å^3, bond length distortion indices of 0.000 (0.022) and 0.002 (0.018), quadratic elongations of 1.000 (1.003) and 1.000 (1.001), bond angle variances of 0.5$^{\circ 2}$ (8.6$^{\circ 2}$) and 0.4$^{\circ 2}$ (3.6$^{\circ 2}$), and effective coordinations of 4.00 (3.93) and 4.00 (3.93), respectively. These values indicate that polyhedral distortion in $Zr_2(WO_4)(PO_4)_2$ occurs mostly through angular distortion of the ZrO_6 octahedral units, which exhibit the largest bond angle variance, whereas the smaller WO_4 and PO_4 tetrahedral units remain nearly ideal (bond length distortion indices close to zero and bond angle variances of $\leq 0.5^{\circ 2}$). In addition, the systematically larger values of bond angle variances and bond length distortion indices in the observed structure, compared to the present PBEsol results, suggest that some minor residual (micro)stresses or imperfections might persist in the crystal structure characterized in the room temperature powder XRD experiments.

By comparison, in α-ZrW_2O_8, the optimized (measured) ZrO_6 octahedra have a volume of 12.115 (11.952) Å^3, a bond length distortion index of 0.014 (0.018), a quadratic elongation of 1.001 (1.001), a bond angle variance of 3.7$^{\circ 2}$ (3.3$^{\circ 2}$), and an effective coordination of 5.96 (5.92). The computed (measured) $W1O_4$ and $W2O_4$ tetrahedra are characterized by volumes of 2.872 (2.815) and 2.925 (2.759) Å^3, bond length distortion indices of 0.019 (0.016) and 0.010 (0.017), quadratic elongations of 1.028 (1.021) and 1.000 (1.001), bond angle variances of 77.6$^{\circ 2}$ (61.0$^{\circ 2}$) and 0.0$^{\circ 2}$ (0.0$^{\circ 2}$), and effective coordinations of 3.91 (3.94) and 3.98 (3.94), respectively.

2.2. Thermodynamic Properties. Phonon calculations were conducted within the quasi-harmonic approximation (QHA) to predict the isobaric thermal properties of the orthorhombic $Zr_2(WO_4)(PO_4)_2$. As a part of the anharmonic effect,[47] a volume dependence of phonon frequencies was introduced within the QHA. A temperature effect was added to the total energy $U(V)$ of the system through the phonon contribution, F_{phonon}, calculated at constant volume as a function of the temperature T, that is,

Table 2. Selected Bond Distances (Å) and Angles (deg) of $Zr_2(WO_4)(PO_4)_2$ (Space Group *Pbcn*, IT No. 60; Z = 4) Calculated with DFT and Measured Using Room Temperature Powder XRD

	O1	O2	O3	O4	O5	O6
Zr1[a]	2.141	2.038	2.063	2.051	2.167	2.049
Zr1[b]	2.186(13)	2.039(12)	2.045(12)	2.042(10)	2.149(13)	2.060(16)
W1[a]	1.784	1.784			1.783	1.783
W1[b]	1.728(13)	1.728(13)			1.806(12)	1.806(12)
P1[a]		1.537	1.531	1.537		1.543
P1[b]		1.491(12)	1.541(12)	1.514(12)		1.456(16)
O−W−O[a]	109.1	110.4	109.0			
O−W−O[b]	110.8(9)	111.8(6)	105.7(5)			
O−P−O[a]	110.4	108.9	108.7	109.2	109.6	109.9
O−P−O[b]	109.3(7)	109.9(8)	109.9(7)	107.8(7)	107.2(7)	112.5(8)
W−O−Zr[a]	169.8					
W−O−Z[b]	164.6(7)					
Zr−O−P[a]	155.9	175.0				
Zr−O−P[b]	155.7(8)	175.6(7)				

[a] This study. [b] Evans et al.; ref 31; powder XRD.

$$F_{\text{phonon}}(T) = \frac{1}{2}\sum_{\mathbf{q},\nu} \hbar\omega_{\mathbf{q},\nu} + k_B T \sum_{\mathbf{q},\nu} \ln[1 - e^{-\beta\hbar\omega_{\mathbf{q},\nu}}] \tag{1}$$

where ν and $\mathbf{q}$ are the band index and wave vector, respectively, $\hbar$ is the reduced Planck constant, $\hbar\omega_{\mathbf{q},\nu}$ is the energy of a single phonon with angular frequency $\omega_{\mathbf{q},\nu}$, T is the temperature of the system, k_B is the Boltzmann constant, and $\beta = (k_B T)^{-1}$.

The thermal variation of the $U(V) + F_{\text{phonon}}(T;V)$ energy as a function of the orthorhombic $Zr_2(WO_4)(PO_4)_2$ unit-cell volume calculated with DFPT in the temperature range $T = 0$–950 K is displayed in Figure 3. The variation of the locus of points corresponding to the local free energy curve (represented by red circles at 10 K intervals in Figure 3) shows a slight initial contraction in unit-cell volume as the temperature increases, followed by typical thermal expansion at higher temperature.

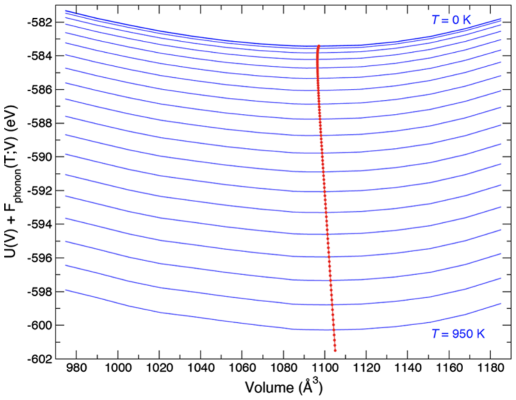

Figure 3. Variation of the total energy with phonon contribution, $U(V) + F_{\text{phonon}}(T;V)$, of orthorhombic $Zr_2(WO_4)(PO_4)_2$ as a function of the unit-cell volume calculated with DFPT at the GGA/PBEsol level from $T = 0$–950 K, at 50 K intervals. Local free energy minima are indicated by red circles, at 10 K intervals.

A volume dependence of the thermodynamic functions needs to be introduced through a transformation to determine the thermal properties of $Zr_2(WO_4)(PO_4)_2$ at constant pressure. This is achieved by defining the Gibbs free energy at constant pressure as follows

$$G(T, P) = \min_V [U(V) + F_{\text{phonon}}(T;V) + PV] \tag{2}$$

where $\min_V$ [function of V] corresponds to a unique minimum of the expression between brackets with respect to the volume V, and U and P are the total energy and pressure of the system. $F_{\text{phonon}}(T;V)$ and $U(V)$ were computed with DFPT/DFT, and the thermodynamic functions of the right-hand side of eq 2 were fitted to the integral form of the universal Vinet[48] equation of state (EoS). The Vinet EoS is defined as

$$P(V) = 3K_0 \frac{(1-x)}{x^2} \exp\left[\frac{3}{2}(K_0' - 1)(1 - x)\right] \tag{3}$$

where P corresponds to the uniform hydrostatic pressure, V_0 and V are the reference and deformed cell volumes, respectively, and where K_0 and K_0' are the bulk modulus and its first derivative with respect to the pressure, expressed as

$$K_0(T) = -V\left(\frac{\partial P}{\partial V}\right)_{P=0} \text{ and } K_0'(T) = \left(\frac{\partial K}{\partial P}\right)_{P=0} \tag{4}$$

with

$$x = \left(\frac{V}{V_0}\right)^{1/3} \tag{5}$$

The bulk modulus values for single-crystal $Zr_2(WO_4)(PO_4)_2$ calculated using the Vinet EoS [eqs 3–5] at $T = 0$ and 300 K are $K_0 = 62.9$ and 63.6 GPa, respectively, close to the experimental estimate of 61.3(8) at $T = 296$ K, reported by Cetinkol and Wilkinson[34] using a 3rd order Birch–Murnaghan (BM) EoS to fit measured unit-cell volumes. However, these predicted values appear significantly larger than the other experimental value of 49(2) GPa estimated by Cetinkol et al.[41] using a BM EoS (Figure 4).

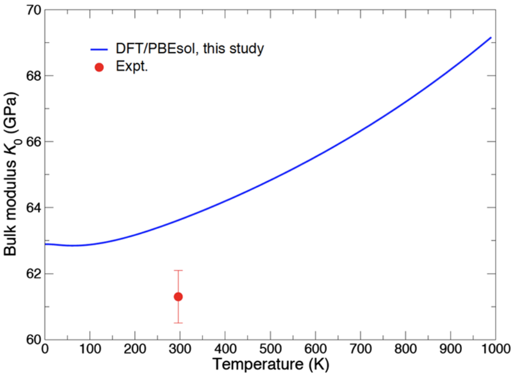

Figure 4. Thermal evolution of the bulk modulus, K_0, for $Zr_2(WO_4)(PO_4)_2$ calculated using the Vinet EoS with DFPT/PBEsol. The experimental estimate from Cetinkol and Wilkinson (ref 34) at $T = 296$ K is also depicted.

For the sake of comparison, the bulk modulus for polycrystalline $Zr_2(WO_4)(PO_4)_2$ was estimated to be 75.0 GPa within the Voigt–Reuss–Hill (VRH) approximations. As described in Supporting Information, this value was obtained from the elastic constants calculated at $T = 0$ K with DFPT as the second derivative of the energy with respect to the strain. The nine independent elastic constants in the stiffness matrix calculated with DFPT/PBEsol for the orthorhombic $Zr_2(WO_4)(PO_4)$ structure are: $C_{11} = 150.0$ GPa, $C_{22} = 100.9$ GPa, $C_{33} = 139.4$ GPa, $C_{44} = 31.4$ GPa, $C_{55} = 51.6$ GPa, $C_{66} = 29.8$ GPa, $C_{12} = 39.4$ GPa, $C_{13} = 76.6$ GPa, and $C_{23} = 39.0$ GPa. The orthorhombic $Zr_2(WO_4)(PO_4)$ structure appears to be mechanically stable because the Born stability conditions[49,50] are satisfied (cf. Supporting Information). As shown in Table 3, these values are relatively close to the elastic constants predicted for cubic α-ZrW_2O_8 at $T = 0$ K with DFPT/PBEsol. Let us note that, although the VRH polycrystalline bulk modulus is slightly larger than its corresponding single-crystal value for $Zr_2(WO_4)(PO_4)_2$, it remains appreciably smaller than the VRH value of 105.7 GPa obtained at the same level of theory for polycrystalline α-ZrW_2O_8.

In addition, the VRH shear (G) and Young's (E) moduli, Poisson's ratio (ν), Vickers microhardness (H_v), and Debye temperature (θ_D) for polycrystalline $Zr_2(WO_4)(PO_4)_2$ were computed from elastic constants (see Table 3 and Supporting Information). The predicted shear modulus of $G = 37.2$ GPa is close to the value of 34.4 GPa obtained for α-ZrW_2O_8 with DFPT/PBEsol.[43] The calculated Young's modulus—representing the ratio of stress to strain—of $E = 95.7$ GPa is also close to the computed[43] and measured[24] values of 93.2 and 98.8 GPa

Table 3. Elastic Constants (C_{ij} in GPa) of polycrystalline $Zr_2(WO_4)(PO_4)_2$ Calculated at $T = 0$ K at the GGA/PBEsol Level and Bulk (K in GPa), Shear (G in GPa), and Young's (E in GPa) Moduli, Poisson's Ratio (ν), Vickers Microhardness (H_v in GPa), and Debye Temperature (θ_D in K) Derived within the VRH Approximation[a]

	$Zr_2(WO_4)(PO_4)_2$				α-ZrW_2O_8	
	DFT[b]	expt[c]	expt[d]	expt[e]	DFT[f]	expt[g]
C_{11}	150.0				162.8	161.8
C_{22}	100.9					
C_{33}	139.4					
C_{44}	31.4				29.8	29.4
C_{55}	51.6					
C_{66}	29.8					
C_{12}	39.4				77.2	75.5
C_{13}	76.6					
C_{23}	39.0					
K	75.0		61.3(8)	49(2)	105.7	104.3
G	37.2				34.4	36.8
E	95.7	74			93.2	98.8
ν	0.287	0.25			0.353	0.342
H_v	4.3	4.4				
θ_D	413				337	333

[a] GGA/PBEsol calculations and experimental estimates for α-ZrW_2O_8 are reported for comparison. [b] This study. [c] Isobe et al., 2009; ref 33; $T \approx 300$ K. [d] Cetinkol and Wilkinson, 2009; ref 34; $T = 296$ K. [e] Cetinkol et al., 2009; ref 41; $T = 300$ K. [f] Weck et al., 2018; ref 43. [g] Drymiotis et al., 2004; ref 24; resonant-ultrasound spectroscopy at $T \approx 0$ K.

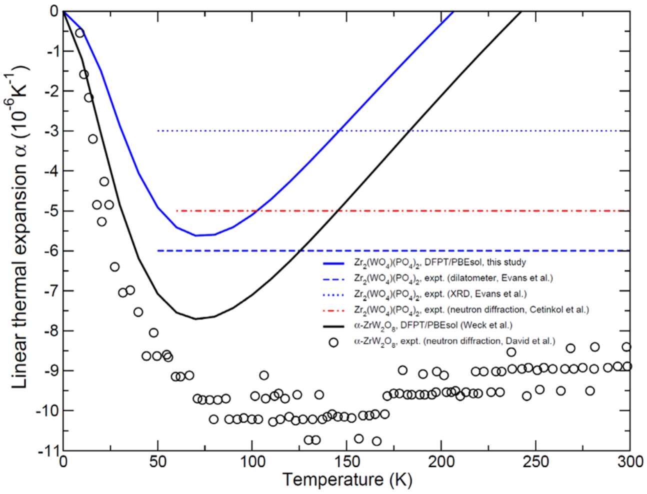

Figure 5. Linear CTE of orthorhombic $Zr_2(WO_4)(PO_4)_2$ computed with DFPT at the GGA/PBEsol level within the QHA. Mean linear CTE values for $Zr_2(WO_4)(PO_4)_2$ from the dilatometer and XRD measurements in the range 50−450 K (ref 32) and from neutron diffraction data in the range 60−300 K (ref 34) are displayed as horizontal lines. DFPT results for single crystal α-ZrW_2O_8 (ref 43) and linear CTE estimates (circles) from high-resolution neutron diffraction data for polycrystalline ZrW_2O_8 (ref 18) are also represented for comparison.

for α-ZrW_2O_8, although it is ∼29% larger than the experimental estimate of 74 GPa determined by Isobe et al.[33] Such a large discrepancy might stem in part from the density (95% of the theoretical density) and the presence of MgO additive contained in the $Zr_2(WO_4)(PO_4)_2$ samples characterized experimentally by Isobe et al.[33] Nevertheless, the calculated Poisson's ratio of $\nu = 0.287$ and Vickers microhardness (i.e., the material's ability to resist plastic deformation) of $H_v = 4.3$ GPa are in good agreement with the experimental values of 0.25 and 4.4 GPa, respectively, reported by Isobe et al.[33] Poisson's ratio provides a measure of the malleability of crystalline compounds;[51] the Poisson's ratio is close to 1/3 for ductile materials, whereas for brittle materials, it is generally much less than 1/3. Therefore, $Zr_2(WO_4)(PO_4)_2$ can be considered ductile, although slightly less ductile than α-ZrW_2O_8, which features larger computed and measured Poisson's ratios of 0.353 and 0.342, respectively. The Debye temperature for polycrystalline $Zr_2(WO_4)(PO_4)_2$ is predicted to be $\theta_D = 413$ K, suggesting a higher microhardness[52] than α-ZrW_2O_8, which exhibits lower calculated[43] and measured[24] Debye temperatures of 337 and 333 K, respectively.

Figure 5 shows the variation with temperature of the linear CTE of orthorhombic $Zr_2(WO_4)(PO_4)_2$ computed with DFPT/PBEsol within the QHA, along with the mean linear CTE values for $Zr_2(WO_4)(PO_4)_2$ from the dilatometer and XRD measurements in the range 50−450 K[32] and from neutron diffraction data in the range 60−300 K.[34] Previous DFPT linear CTE results[43] for single crystal α-ZrW_2O_8 and linear CTE estimates from high-resolution neutron diffraction data[18] for polycrystalline ZrW_2O_8 are also represented for comparison. As discussed in our previous DFPT/PBEsol study of NTE α-ZrW_2O_8, the linear CTE results obtained with DFPT/PBEsol within the QHA depart significantly from the experimental data above ∼70 K, therefore the calculated linear CTE results for $Zr_2(WO_4)(PO_4)_2$ are shown for only up to room temperature (see ref 43 for details). The linear CTE was calculated using the expression $\alpha_L = V_0^{-1/3}\Delta(V^{1/3})/\Delta T$, where the reference crystal cell volume, V_0, corresponds to the temperature $T = 0$ K and $\Delta(V^{1/3})/\Delta T$ is the variation of the cell volume with temperature. As discussed above (see Figure 3), the volume dependence of the phonon free energy varies with temperature, resulting in a temperature-dependent equilibrium volume of $Zr_2(WO_4)(PO_4)_2$, which can be assimilated into thermal expansion within the QHA approach. As depicted in Figure 5, the computed linear CTE for $Zr_2(WO_4)(PO_4)_2$ reaches an extremum of -5.6×10^{-6} K^{-1} at ∼70 K, and NTE persists below 207 K. Similar behavior was predicted with DFPT/PBEsol for single-crystal α-ZrW_2O_8, reaching an extremum of -7.7×10^{-6} K^{-1} near ∼70 K and exhibiting NTE below 242 K.[43] In previous studies of α-ZrW_2O_8, discrepancies were found above ∼60−70 K between experimental NTE data for polycrystalline samples[18] and DFT/B3LYP or DFPT/PBEsol calculations of ideal single-crystal α-ZrW_2O_8 models[43,46] (see Figure 5). Such differences were attributed in part to the creation of thermally induced defects in real samples and might also be ascribed to inherent limitations of the QHA approach, which fails to accurately account for explicit/true anharmonicity. The mean linear CTE calculated here for orthorhombic single-crystal $Zr_2(WO_4)(PO_4)_2$ is -3.1×10^{-6} K^{-1} in the temperature range ∼0−70 K. This value is in good agreement with the mean linear CTE of -3×10^{-6} K^{-1} measured by Evans et al.[32] using XRD measurements in the temperature range ∼50−450 K, although only half of the value of -6×10^{-6} K^{-1} reported by these authors using dilatometer data was over the same temperature range and smaller than the estimate of -5×10^{-6} K^{-1} as reported by Cetinkol and Wilkinson[34] from neutron diffraction data between 60 and 300 K. Other recent experimental mean linear CTE estimates above room temperature are consistent with the value calculated in this study at low temperature. For example, Isobe and coworkers[33] measured a value of -3.4×10^{-6} K^{-1} in the range ~300−875 K, and Liu et al.[36] reported values of -2.36×10^{-6} and -2.61×10^{-6} K^{-1} in the temperature range ~300−1000 K for $Zr_2(WO_4)(PO_4)_2$ samples sintered at 1573 and 1673 K, respectively. It is important to note that, as mentioned in the Introduction section, differences in the CTE for $Zr_2(WO_4)(PO_4)_2$ can be attributed to different porosities or average grain sizes resulting from sintering conditions and/or synthesis reactions and to possible pressure-induced phase transformations during sample fabrication.

The vibrational theory of thermal expansion formulated by Grüneisen[53,54] was utilized to calculate the thermal evolution of the mean Grüneisen parameter γ of $Zr_2(WO_4)(PO_4)_2$, as well as the mode Grüneisen parameters as functions of frequency, represented in Figure 6. Within this theoretical framework, the thermal expansion of materials is given by $\alpha_L = \sum_i \alpha_i = \gamma C_V/3K$, where C_V is the specific heat capacity, K is the bulk modulus, and γ is the mean Grüneisen parameter expressed as $\gamma = \sum_i \gamma_i c_i / \sum_i c_i$, where the mode Grüneisen parameters given by $\gamma_i = -\partial \ln \omega_i / \partial \ln V$ represent the relative change of mode frequencies, ω_i with crystal cell volume V and c_i are the contributions of these vibrational modes to the total specific heat C_V.

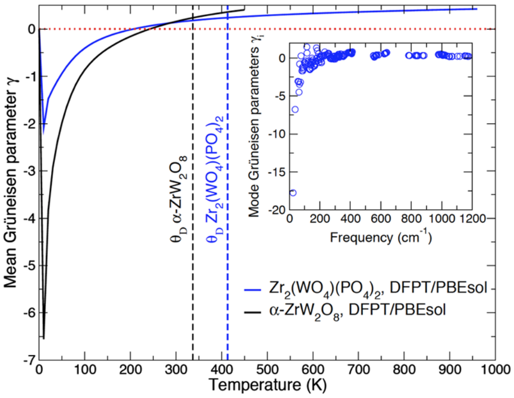

Figure 6. Thermal evolution of the mean Grüneisen parameter, γ, of $Zr_2(WO_4)(PO_4)_2$ calculated using DFPT at the GGA/PBEsol level within the QHA. Corresponding GGA/PBEsol results for α-ZrW_2O_8 (ref 43) are also displayed. Calculated Debye temperatures, θ_D, are represented by vertical dashed lines. Inset: Calculated mode Grüneisen parameters of $Zr_2(WO_4)(PO_4)_2$ as functions of frequency.

In the expression of the thermal expansion $\alpha_L = \gamma C_V/3K$, both the bulk modulus and the specific heat are positive, therefore, the mean Grüneisen parameter, γ, is the parameter controlling the positive or negative thermal expansion, with the NTE originating from vibrational modes with $\gamma_i < 0$. As shown in Figure 6, the mean Grüneisen parameter of $Zr_2(WO_4)(PO_4)_2$ calculated with DFPT/PBEsol is negative below 205 K, with a minimum of −2.1 at 10 K. At the same level of theory, γ was predicted to be negative below 245 K for α-ZrW_2O_8, with a minimum of −6.56 at 10 K. Despite being positive above 205 K, γ for $Zr_2(WO_4)(PO_4)_2$ remains close to zero up to its Debye temperature of 413 K, which is the temperature above which most vibrational modes of the crystal are fully excited. Therefore, phonon modes have little to no net effect on the lattice expansion between ~205 and 413 K. Similarly, David et al.[18] observed that phonon modes play a very limited role in the lattice expansion of α-ZrW_2O_8 in the temperature range of ~300−550 K. A closer examination of the computed mode Grüneisen parameters of $Zr_2(WO_4)(PO_4)_2$ (see inset in Figure 6) reveals that the two lowest-frequency optical phonons at 24 cm^{-1} ($\gamma_1 = -17.7$) and 38 cm^{-1} ($\gamma_2 = -6.8$) contribute mainly to NTE, along with numerous phonon modes with $\gamma_i < 0$ below ~300 K. Although a full analysis of the phonon modes is beyond the scope of the present study and will be the focus of a forthcoming investigation, preliminary analysis suggests that both the lowest-temperature modes are characterized by variations of intrapolyhedral bond angles O−M−O (M = W, Zr), with relatively limited M−O bond distance variation. These results are consistent with the findings for α-ZrW_2O_8 showing that both the lowest-frequency optical phonons, predicted at 36 cm^{-1} (T_{irrep}) and 37 cm^{-1} (E_{irrep}) with PBEsol,[43] are responsible for most of the low temperature NTE, that is, up to ~70% of the CTE in the vicinity of 30 K according to the Debye−Einstein QHA calculations.[46] Intrapolyhedral bond angle O−M−O variations for these lowest-frequency vibrational modes of α-ZrW_2O_8 were achieved through libration/translation of WO_4 building blocks.

Lattice vibration contributions from phonon calculations were used to derive thermodynamic functions fitted to the Vinet EoS. The electronic contribution to the thermodynamic properties is negligible because the band gap computed with PBEsol for orthorhombic $Zr_2(WO_4)(PO_4)_2$ is 3.20 eV, that is, comparable to the value of 3.45 eV obtained for α-ZrW_2O_8 at the same level of theory.[43] Within the QHA, the molar isobaric heat capacity, C_P, was calculated as a function of temperature and pressure according to

$$\begin{aligned} C_P(T, P) &= -T\frac{\partial^2 G(T, P)}{\partial T^2} \\ &= T\frac{\partial V(T, P)}{\partial T}\frac{\partial S(T;V)}{\partial V}\bigg|_{V=V(T,P)} \\ &\quad + C_V[T, V(T, P)] \end{aligned} \tag{6}$$

where $V(T,P)$ is the equilibrium volume at T and P, and the pressure is set to the reference ambient pressure for the standard state adopted in calorimetric data, that is, P = 1 bar and where the molar entropy, S, is expressed as

$$S = -k_B \sum_{\mathbf{q},\nu} \ln[1 - e^{-\beta\hbar\omega_{\mathbf{q},\nu}}] - \frac{1}{T}\sum_{\mathbf{q},\nu} \frac{\hbar\omega_{\mathbf{q},\nu}}{e^{\beta\hbar\omega_{\mathbf{q},\nu}} - 1} \tag{7}$$

with the molar isochoric heat capacity, C_V, given by

$$C_V = k_B \sum_{\mathbf{q},\nu} (\beta\hbar\omega_{\mathbf{q},\nu})^2 \frac{e^{\beta\hbar\omega_{\mathbf{q},\nu}}}{[e^{\beta\hbar\omega_{\mathbf{q},\nu}} - 1]^2} \tag{8}$$

where the remaining variables in eqs 6−8 have been defined in eqs 1 and 2. The molar isochoric capacity and isobaric heat capacity calculated at constant atmospheric pressure for $Zr_2(WO_4)(PO_4)_2$ are displayed in Figure 7, along with C_P lattice dynamics results for α-ZrW_2O_8 calculated up to ~431 K (i.e., the temperature corresponding to the $\alpha \to \beta$ structural phase transition in ZrW_2O_8) using DFPT/PBEsol within the QHA.[43] The computed standard molar heat capacity of $Zr_2(WO_4)(PO_4)_2$ at T = 298.15 K is C_P^0 = 287.6 J·mol^{-1}·K^{-1}, which is significantly larger than the corresponding value of C_P^0 = 192.2 J·mol^{-1}·K^{-1} calculated for α-ZrW_2O_8. At 960 K, the

DOI: 10.1021/acsomega.8b02456
ACS Omega 2018, 3, 15780−15788

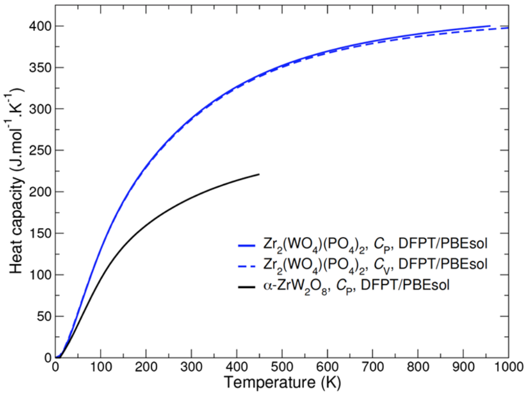

Figure 7. Molar isochoric (C_V) and isobaric (C_P) heat capacities of $Zr_2(WO_4)(PO_4)_2$ calculated at constant atmospheric pressure using DFPT at the GGA/PBEsol level within the QHA. C_P results for α-ZrW_2O_8 calculated with GGA/PBEsol (ref 43) are also displayed for comparison.

highest temperature considered in this study for C_P, the difference between the calculated C_P and C_V remains small, that is, only ~4 J·mol^{-1}·K^{-1}. At this temperature, C_P is only ~6% below its theoretical Dulong−Petit asymptotic value of $C_P = 3n\text{R} = 424.0$ J·mol^{-1}·K^{-1}, where n is the number of atoms per formula unit and R (8.314 J·mol^{-1}·K^{-1}) is the universal gas constant.

Figure 8 shows the thermal evolution of the molar entropy of $Zr_2(WO_4)(PO_4)_2$ calculated at equilibrium volume with eq 7 using DFPT/PBEsol. The calculated molar entropy features the typical logarithmic increase according to the Boltzmann's entropy formula, $S = k_B \cdot \log(W)$, where W is the number of microstates in the system. The standard molar entropy is predicted to be $S^0 = 321.9$ J·mol^{-1}·K^{-1} at $T = 298.15$ K, that is appreciably larger than the corresponding value of 229.2 J·mol^{-1}·K^{-1} predicted for α-ZrW_2O_8 at the same level of theory.

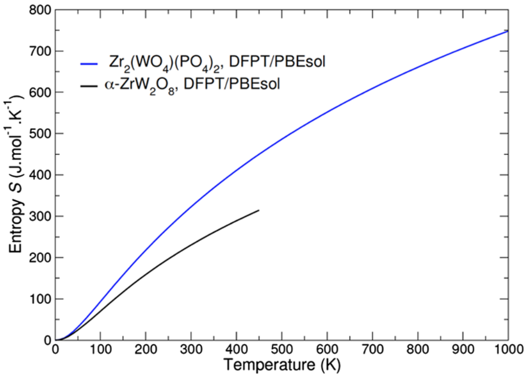

Figure 8. Molar entropy of $Zr_2(WO_4)(PO_4)_2$ calculated at equilibrium volume using DFPT at the GGA/PBEsol level. The molar entropy of α-ZrW_2O_8 calculated at the same level of theory is represented (ref 43).

3. CONCLUSIONS

Using DFPT with the PBEsol XC functional, the crystal structure, phonon, and thermomechanical properties of the orthorhombic NTE material $Zr_2(WO_4)(PO_4)_2$ have been investigated computationally for the first time. The results obtained for $Zr_2(WO_4)(PO_4)_2$ with this approach have been systematically and extensively compared with the available experimental data for this material, as well as with previous results for the notorious α-ZrW_2O_8 NTE compound.

The $Zr_2(WO_4)(PO_4)_2$ structure optimized with GGA/PBEsol at $T = 0$ K possesses crystal unit-cell parameters of $a = 9.432$, $b = 12.432$, and $c = 9.250$ Å, with a unit-cell volume ~2.3% larger than the estimate of $V = 1059.34(4)$ Å^3 obtained at $T = 60$ K by Cetinkol and Wilkinson using neutron diffraction data.

The bulk modulus predicted for $Zr_2(WO_4)(PO_4)_2$ using the Vinet EoS is $K_0 = 63.6$ GPa at room temperature, which is in close agreement with the experimental estimate of 61.3(8) at $T = 296$ K. At $T = 0$ K, the nine independent elastic constants in the stiffness matrix calculated with DFPT/PBEsol for the orthorhombic $Zr_2(WO_4)(PO_4)$ structure are: $C_{11} = 150.0$ GPa, $C_{22} = 100.9$ GPa, $C_{33} = 139.4$ GPa, $C_{44} = 31.4$ GPa, $C_{55} = 51.6$ GPa, $C_{66} = 29.8$ GPa, $C_{12} = 39.4$ GPa, $C_{13} = 76.6$ GPa, and $C_{23} = 39.0$ GPa. The VRH shear and Young's moduli, Poisson's ratio, Vickers microhardness, and Debye temperature for polycrystalline $Zr_2(WO_4)(PO_4)_2$ were computed from elastic constants, that is, $G = 37.2$ GPa, $E = 95.7$ GPa, $\nu = 0.287$, $H_v = 4.3$ GPa, and $\theta_D = 413$ K, respectively.

The computed mean linear CTE is -3.1×10^{-6} K^{-1} in the temperature range ~0−70 K, in line with the mean linear CTE of -3×10^{-6} K^{-1} measured by Evans et al. using XRD measurements in the temperature range ~50−450 K. The mean Grüneisen parameter controlling the thermal expansion of $Zr_2(WO_4)(PO_4)_2$ is negative below 205 K, with a minimum of −2.1 at 10 K. The calculated standard molar heat capacity and entropy are $C_P^0 = 287.6$ and $S^0 = 321.9$ J·mol^{-1}·K^{-1}, respectively.

Results reported in this study show that the DFPT/PBEsol computational approach is sufficiently accurate for assessing or predicting the relationship between structural and thermomechanical properties of NTE materials.

4. METHODS

4.1. Computational Methods. First-principles calculations were performed using DFT/DFPT implemented in the Vienna Ab initio Simulation package[55] (VASP). The XC energy was computed using the GGA with the Perdew, Burke, and Ernzerhof parameterization revised for solids (PBEsol).[42] The PBEsol XC functional showed superior accuracy over standard functionals, such as PBE, in previous computational studies of the NTE material α-ZrW_2O_8.[43,44] The accuracy of our DFT/DFPT computational approach was extensively tested in previous lattice dynamics studies.[52,56−60]

The projector augmented wave (PAW) method[61,62] was utilized to describe the interaction between valence electrons and ionic cores. The O($2s^2$,$2p^4$), P($3s^2$,$3p^3$), W($6s^2$,$5d^4$), and Zr($4p^6$,$5s^2$,$4d^2$) electrons were treated explicitly as valence electrons in the Kohn−Sham (KS) equations, and the remaining core electrons together with the nuclei were represented by PAW pseudopotentials. The KS equation was solved using the blocked Davidson[63] iterative matrix diagonalization scheme. The plane-wave cutoff energy for the electronic wavefunctions was set to 500 eV, ensuring the total energy of the system to be converged to within 1 meV/atom.

A 3D-periodic unit-cell approach was utilized, with the orthorhombic crystal unit cell of $Zr_2(WO_4)(PO_4)_2$ [space group *Pbcn*, IT no. 60, setting no. 3 *Pnca* (c, a, b); $Z = 4$] solved by Evans et al.[31] chosen as the initial structure in relaxation calculations. Because of the large size of the unit cell (68 atoms, $V_0 = 1056.34$ Å^3), a k-point mesh of 5 × 5 × 5 was utilized to sample the Brillouin zone using the Monkhorst–Pack k-point scheme.[64] Unit-cell relaxation calculations were initially carried out until the Hellmann–Feynman forces acting on atoms were converged within 0.01 eV/Å, without symmetry constraints imposed. The structure optimized from total-energy minimization was then relaxed with respect to Hellmann–Feynman forces with a convergence tolerance set to 0.001 eV/Å, and DFPT linear response calculations were carried out with VASP to determine the phonon frequencies and elastic properties. Using the QHA—which introduces a volume dependence of phonon frequencies as a part of the anharmonic effect[47]—the thermal properties of $Zr_2(WO_4)(PO_4)_2$ were derived from phonon calculations. This computational approach was validated in previous studies to successfully predict the properties of various Zr-containing compounds and crystalline materials.[52,56–58,65–68]

■ ASSOCIATED CONTENT

Ⓢ Supporting Information

The Supporting Information is available free of charge on the ACS Publications website at DOI: 10.1021/acsomega.8b02456.

> Computational methods utilized to obtain elastic constants, shear and Young's moduli, Poisson's ratio, Vickers microhardness, Debye temperature, and Born stability conditions (PDF)

■ AUTHOR INFORMATION

Corresponding Author

*E-mail: pfweck@sandia.gov. Phone: 505-844-8144 (P.F.W.).

ORCID

Philippe F. Weck: 0000-0002-7610-2893

Jeffery A. Greathouse: 0000-0002-4247-3362

Notes

The authors declare no competing financial interest.

■ ACKNOWLEDGMENTS

Sandia National Laboratories is a multimission laboratory managed and operated by National Technology and Engineering Solutions of Sandia, LLC., a wholly owned subsidiary of Honeywell International, Inc., for the U.S. Department of Energy's National Nuclear Security Administration under contract DE-NA0003525. This work was supported by Laboratory Directed Research and Development (LDRD) funding from Sandia National Laboratories. This work was performed, in part, at the Center for Integrated Nanotechnologies, an Office of Science User Facility operated for the U.S. Department of Energy (DOE) Office of Science. The views expressed in the article do not necessarily represent the views of the U.S. DOE or the United States Government.

■ REFERENCES

(1) Chu, C. N.; Saka, N.; Suh, N. P. Negative Thermal Expansion Ceramics: A Review. *Mater. Sci. Eng.* **1987**, *95*, 303–308.

(2) Roy, R.; Agrawal, D. K.; McKinstry, H. A. Very Low Thermal Expansion Coefficient Materials. *Annu. Rev. Mater. Sci.* **1989**, *19*, 59–81.

(3) White, G. K. Solids: Thermal Expansion and Contraction. *Contemp. Phys.* **1993**, *34*, 193–204.

(4) Sleight, A. W. Isotropic Negative Thermal Expansion. *Annu. Rev. Mater. Sci.* **1998**, *28*, 29–43.

(5) Evans, J. S. O. Negative thermal expansion materials. *J. Chem. Soc., Dalton Trans.* **1999**, 3317–3326.

(6) Barrera, G. D.; Bruno, J. A. O.; Barron, T. H. K.; Allan, N. L. Negative Thermal Expansion. *J. Phys.: Condens. Matter* **2005**, *17*, R217–R252.

(7) Takenaka, K. Negative Thermal Expansion Materials: Technological Key for Control of Thermal Expansion. *Sci. Technol. Adv. Mater.* **2012**, *13*, 013001.

(8) Lind, C. Two Decades of Negative Thermal Expansion Research: Where Do We Stand? *Materials* **2012**, *5*, 1125–1154.

(9) Dove, M. T.; Fang, H. Negative Thermal Expansion and Associated Anomalous Physical Properties: Review of the Lattice Dynamics Theoretical Foundation. *Rep. Prog. Phys.* **2016**, *79*, 066503.

(10) Kittel, C. *Introduction to Solid State Physics*, 7th ed.; Wiley: New York, 1996.

(11) Korthuis, V.; Khosrovani, N.; Sleight, A. W.; Roberts, N.; Dupree, R.; Warren, W. W. Negative Thermal Expansion and Phase Transitions in the $ZrV_{2-x}P_xO_7$ Series. *Chem. Mater.* **1995**, *7*, 412–417.

(12) Auray, M.; Quarton, M.; Leblanc, M. Zirconium Tungstate. *Acta Crystallogr., Sect. C: Cryst. Struct. Commun.* **1995**, *51*, 2210–2213.

(13) Mary, T. A.; Evans, J. S. O.; Vogt, T.; Sleight, A. W. Negative Thermal Expansion from 0.3 to 1050 Kelvin in ZrW_2O_8. *Science* **1996**, *272*, 90–92.

(14) Evans, J. S. O.; Mary, T. A.; Vogt, T.; Subramanian, M. A.; Sleight, A. W. Negative Thermal Expansion in ZrW_2O_8 and HfW_2O_8. *Chem. Mater.* **1996**, *8*, 2809–2823.

(15) Evans, J. S. O.; Hu, Z.; Jorgensen, J. D.; Argyriou, D. N.; Short, S.; Sleight, A. W. Compressibility, Phase Transitions, and Oxygen Migration in Zirconium Tungstate, ZrW_2O_8. *Science* **1997**, *275*, 61–65.

(16) Evans, J. S. O.; David, W. I. F.; Sleight, A. W. Structural investigation of the negative-thermal-expansion material ZrW_2O_8. *Acta Crystallogr., Sect. B: Struct. Sci.* **1999**, *55*, 333–340.

(17) Ernst, G.; Broholm, C.; Kowach, G. R.; Ramirez, A. P. Phonon density of states and negative thermal expansion in ZrW_2O_8. *Nature* **1998**, *396*, 147–149.

(18) David, W. I. F.; Evans, J. S. O.; Sleight, A. W. Direct evidence for a low-frequency phonon mode mechanism in the negative thermal expansion compound ZrW_2O_8. *Europhys. Lett.* **1999**, *46*, 661–666.

(19) Perottoni, C. A.; da Jornada, J. A. H. Pressure-Induced Amorphization and Negative Thermal Expansion in ZrW_2O_8. *Science* **1998**, *280*, 886–889.

(20) Ramirez, A. P.; Kowach, G. R. Large Low Temperature Specific Heat in the Negative Thermal Expansion Compound ZrW_2O_8. *Phys. Rev. Lett.* **1998**, *80*, 4903–4906.

(21) Yamamura, Y.; Nakajima, N.; Tsuji, T. Heat capacity anomaly due to the α-to-β structural phase transition in ZrW_2O_8. *Solid State Commun.* **2000**, *114*, 453–455.

(22) Ravindran, T. R.; Arora, A. K.; Mary, T. A. High Pressure Behavior of ZrW_2O_8: Grüneisen Parameter and Thermal Properties. *Phys. Rev. Lett.* **2000**, *84*, 3879–3882.

(23) Ravindran, T. R.; Arora, A. K.; Mary, T. A. High-Pressure Raman Spectroscopic Study of Zirconium Tungstate. *J. Phys.: Condens. Matter* **2001**, *13*, 11573–11588.

(24) Drymiotis, F. R.; Ledbetter, H.; Betts, J. B.; Kimura, T.; Lashley, J. C.; Migliori, A.; Ramirez, A.; Kowach, G.; Van Duijn, J. Monocrystal Elastic Constants of the Negative-Thermal-Expansion Compound Zirconium Tungstate (ZrW_2O_8). *Phys. Rev. Lett.* **2004**, *93*, 025502.

(25) Hancock, J. N.; Turpen, C.; Schlesinger, Z.; Kowach, G. R.; Ramirez, A. P. Unusual Low-Energy Phonon Dynamics in the Negative Thermal Expansion Compound ZrW_2O_8. *Phys. Rev. Lett.* **2004**, *93*, 225501.

(26) Keen, D. A.; Goodwin, A. L.; Tucker, M. G.; Dove, M. T.; Evans, J. S. O.; Crichton, W. A.; Brunelli, M. Structural Description of Pressure-Induced Amorphization in ZrW_2O_8. *Phys. Rev. Lett.* **2007**, *98*, 225501.

(27) Bridges, F.; Keiber, T.; Juhas, P.; Billinge, S. J. L.; Sutton, L.; Wilde, J.; Kowach, G. R. Local Vibrations and Negative Thermal Expansion in ZrW_2O_8. *Phys. Rev. Lett.* **2014**, *112*, 045505.

(28) Stevens, R.; Linford, J.; Woodfield, B. F.; Boerio-Goates, J.; Lind, C.; Wilkinson, A. P.; Kowach, G. Heat capacities, third-law entropies and thermodynamic functions of the negative thermal expansion materials, cubic α-ZrW_2O_8 and cubic $ZrMo_2O_8$, from K. *J. Chem. Thermodyn.* **2003**, *35*, 919−937.

(29) Martinek, C. A.; Hummel, F. A. Subsolidus Equilibria in the System ZrO_2-WO_3-P_2O_5. *J. Am. Ceram. Soc.* **1970**, *53*, 159−161.

(30) Tsvigunov, A. N.; Sirotinkin, V. P. Synthesis and Results of Indicating of $Zr_2WO_4(PO_4)_2$ X-Ray-Films. *Zh. Neorg. Khim.* **1990**, *35*, 3065.

(31) Evans, J. S. O.; Mary, T. A.; Sleight, A. W. Structure of $Zr_2(WO_4)(PO_4)_2$ from Powder X-Ray Data: Cation Ordering with No Superstructure. *J. Solid State Chem.* **1995**, *120*, 101−104.

(32) Evans, J. S. O.; Mary, T. A.; Sleight, A. W. Negative Thermal Expansion in a Large Molybdate and Tungstate Family. *J. Solid State Chem.* **1997**, *133*, 580−583.

(33) Isobe, T.; Umezome, T.; Kameshima, Y.; Nakajima, A.; Okada, K. Preparation and properties of negative thermal expansion $Zr_2WP_2O_{12}$ ceramics. *Mater. Res. Bull.* **2009**, *44*, 2045−2049.

(34) Cetinkol, M.; Wilkinson, A. P. Pressure dependence of negative thermal expansion in $Zr_2(WO_4)(PO_4)_2$. *Solid State Commun.* **2009**, *149*, 421−424.

(35) Shang, R.; Hu, Q.; Liu, X.; Liang, E.; Yuan, B.; Chao, M. Effect of MgO and PVA on the Synthesis and Properties of Negative Thermal Expansion Ceramics of $Zr_2(WO_4)(PO_4)_2$. *Int. J. Appl. Ceram. Technol.* **2013**, *10*, 849−856.

(36) Liu, X.; Wang, J.; Fan, C.; Shang, R.; Cheng, F.; Yuan, B.; Song, W.; Chen, Y.; Liang, E.; Chao, M. Control of Reaction Pathways for Rapid Synthesis of Negative Thermal Expansion Ceramic $Zr_2P_2WO_{12}$ with Uniform Microstructure. *Int. J. Appl. Ceram. Technol.* **2015**, *12*, E28−E33.

(37) Shi, X.; Lian, H.; Qi, R.; Cui, L.; Yao, N. Preparation and properties of negative thermal expansion $Zr_2P_2WO_{12}$ powders and $Zr_2P_2WO_{12}$/TiNi composites. *Mater. Sci. Eng., B* **2016**, *203*, 1−6.

(38) Isobe, T.; Kato, Y.; Mizutani, M.; Ota, T.; Daimon, K. Pressureless sintering of negative thermal expansion ZrW_2O_8/$Zr_2WP_2O_{12}$ composites. *Mater. Lett.* **2008**, *62*, 3913−3915.

(39) Tani, J.-i.; Takahashi, M.; Kido, H. Fabrication and thermal expansion properties of ZrW_2O_8/$Zr_2WP_2O_{12}$ composites. *J. Eur. Ceram. Soc.* **2010**, *30*, 1483−1488.

(40) Yanase, I.; Sakai, H.; Kobayashi, H. Fabrication of $Zr_2WP_2O_{12}$/$ZrV_{0.6}P_{1.4}O_7$ composite with a nearly zero-thermal-expansion property. *Mater. Lett.* **2017**, *207*, 221−224.

(41) Cetinkol, M.; Wilkinson, A. P.; Lind, C. In Situ High-Pressure Synchrotron X-Ray Diffraction Study of $Zr_2(WO_4)(PO_4)_2$ up to 16 GPa. *Phys. Rev. B: Condens. Matter Mater. Phys.* **2009**, *79*, 224118.

(42) Perdew, J. P.; Ruzsinszky, A.; Csonka, G. I.; Vydrov, O. A.; Scuseria, G. E.; Constantin, L. A.; Zhou, X.; Burke, K. Restoring the Density-Gradient Expansion for Exchange in Solids and Surfaces. *Phys. Rev. Lett.* **2008**, *100*, 136406.

(43) Weck, P. F.; Kim, E.; Greathouse, J. A.; Gordon, M. E.; Bryan, C. R. Assessing exchange-correlation functionals for elasticity and thermodynamics of α-ZrW_2O_8: A density functional perturbation theory study. *Chem. Phys. Lett.* **2018**, *698*, 195−199.

(44) Weck, P. F.; Gordon, M. E.; Greathouse, J. A.; Bryan, C. R.; Meserole, S. P.; Rodriguez, M. A.; Payne, C.; Kim, E. Infrared and Raman spectroscopy of α-ZrW_2O_8: A comprehensive density functional perturbation theory and experimental study. *J. Raman Spectrosc.* **2018**, *49*, 1373−1384.

(45) Ramzan, M.; Luo, W.; Ahuja, R. High pressure, mechanical, and optical properties of ZrW_2O_8. *J. Appl. Phys.* **2011**, *109*, 033510.

(46) Gava, V.; Martinotto, A. L.; Perottoni, C. A. First-Principles Mode Grüneisen Parameters and Negative Thermal Expansion in α-ZrW_2O_8. *Phys. Rev. Lett.* **2012**, *109*, 195503.

(47) Togo, A.; Oba, F.; Tanaka, I. First-Principles Calculations of the Ferroelastic Transition Between Rutile-Type and $CaCl_2$-Type SiO_2 at High Pressures. *Phys. Rev. B: Condens. Matter Mater. Phys.* **2008**, *78*, 134106.

(48) Vinet, P.; Rose, J. H.; Ferrante, J.; Smith, J. R. Universal Features of the of State of Solids. *J. Phys.: Condens. Matter* **1989**, *1*, 1941−1963.

(49) Born, M. On the stability of crystal lattices. I. *Proc. Cambridge Philos. Soc.* **1940**, *36*, 160−172.

(50) Born, M.; Huang, K. *Dynamics Theory of Crystal Lattices*; Oxford University Press: Oxford, 1954.

(51) Frantsevich, I. N.; Voronov, F. F.; Bokuta, S. A. *Elastic Constants and Elastic Moduli of Metals and Insulators Handbook*; Frantsevich, I. N., Ed.; Naukova Dumka: Kiev, 1983; p 60.

(52) Weck, P. F.; Kim, E.; Tikare, V.; Mitchell, J. A. Mechanical Properties of Zirconium Alloys and Zirconium Hydrides Predicted from Density Functional Perturbation Theory. *Dalton Trans.* **2015**, *44*, 18769−18779.

(53) Grüneisen, E. Theorie des festen Zustandes einatomiger Elemente. *Ann. Phys.* **1912**, *344*, 257−306.

(54) Grüneisen, E. Zustand des festen Körpers. *Thermische Eigenschaften der Stoffe*; Springer, 1926; Vol. *10*, pp 1−59.

(55) Kresse, G.; Furthmüller, J. Efficient iterative schemes forab initiototal-energy calculations using a plane-wave basis set. *Phys. Rev. B: Condens. Matter Mater. Phys.* **1996**, *54*, 11169−11186.

(56) Weck, P. F.; Kim, E. Assessing Hubbard-corrected AM05+U and PBEsol+U density functionals for strongly correlated oxides CeO_2 and Ce_2O_3. *Phys. Chem. Chem. Phys.* **2016**, *18*, 26816−26826.

(57) Weck, P. F.; Kim, E. Uncloaking the Thermodynamics of the Studtite to Metastudtite Shear-Induced Transformation. *J. Phys. Chem. C* **2016**, *120*, 16553−16560.

(58) Johnson, T. J.; Sweet, L. E.; Meier, D. E.; Mausolf, E. J.; Kim, E.; Weck, P. F.; Buck, E. C.; McNamara, B. K. Time-Resolved Infrared Reflectance Studies of the Dehydration-Induced Transformation of Uranyl Nitrate Hexahydrate to the Trihydrate Form. *J. Phys. Chem. A* **2015**, *119*, 9996−10006.

(59) Weck, P. F.; Kim, E. Layered uranium(VI) hydroxides: structural and thermodynamic properties of dehydrated schoepite α-$UO_2(OH)_2$. *Dalton Trans.* **2014**, *43*, 17191−17199.

(60) Weck, P. F.; Kim, E. Solar Energy Storage in Phase Change Materials: First-Principles Thermodynamic Modeling of Magnesium Chloride Hydrates. *J. Phys. Chem. C* **2014**, *118*, 4618−4625.

(61) Blöchl, P. E. Projector Augmented-Wave Method. *Phys. Rev. B: Condens. Matter Mater. Phys.* **1994**, *50*, 17953−17979.

(62) Kresse, G.; Joubert, D. From Ultrasoft Pseudopotentials to the Projector Augmented-Wave Method. *Phys. Rev. B: Condens. Matter Mater. Phys.* **1999**, *59*, 1758−1775.

(63) Davidson, E. R. *Methods in Computational Molecular Physics*; Diercksen, G. H. F., Wilson, S., Eds.; NATO Advanced Study Institute, Series C, Plenum: New York, 1983; Vol. *113*, p 95.

(64) Monkhorst, H. J.; Pack, J. D. Special Points for Brillouin-Zone Integrations. *Phys. Rev. B: Solid State* **1976**, *13*, 5188−5192.

(65) Colmenero, F.; Bonales, L. J.; Cobos, J.; Timón, V. Thermodynamic and Mechanical Properties of the Rutherfordine Mineral Based on Density Functional Theory. *J. Phys. Chem. C* **2017**, *121*, 5994−6001.

(66) Weck, P. F.; Kim, E.; Buck, E. C. On the Mechanical Stability of Uranyl Peroxide Hydrates: Implications for Nuclear Fuel Degradation. *RSC Adv.* **2015**, *5*, 79090−79097.

(67) Weck, P. F.; Kim, E.; Jové-Colón, C. F. Relationship Between Crystal Structure and Thermo-Mechanical Properties of Kaolinite Clay: Beyond Standard Density Functional Theory. *Dalton Trans.* **2015**, *44*, 12550−12560.

(68) Weck, P. F.; Kim, E. Thermodynamics of Technetium: Reconciling Theory and Experiment Using Density Functional Perturbation Analysis. *Dalton Trans.* **2015**, *44*, 12735−12742.